

Electronic vascular conduit for in situ identification of hemadostenosis and thrombosis in small animals and nonhuman primates

Received: 5 April 2024

Accepted: 11 March 2025

Published online: 18 March 2025

 Check for updates

Zhirong Liu^{1,2,3,6}, Chuyu Tang^{1,2,6}, Nannan Han^{4,6}, Zhuoheng Jiang^{1,2}, Xi Liang^{1,2}, Shaobo Wang¹, Quanhong Hu¹, Cheng Xiong¹, Shuncheng Yao^{1,2}, Zhuo Wang¹, Zhong Lin Wang^{1,2,5}  , Duohong Zou⁴   & Linlin Li^{1,2}  

Patients suffering from coronary artery disease (CAD) or peripheral arterial disease (PAD) can benefit from bypass graft surgery. For this surgery, arterial vascular grafts have become promising alternatives when autologous grafts are inaccessible but suffer from numerous postimplantation challenges, particularly delayed endothelialization, intimal hyperplasia, high risk of thrombogenicity and restenosis, and difficulty in timely detection of these subtle pathological changes. We present an electronic vascular conduit that integrates flexible electronics into bionic vascular grafts for in situ, real-time and long-term monitoring for hemadostenosis and thrombosis concurrent with postoperative vascular repair. Following bypass surgery, the integrated bioelectronic sensor based on the triboelectric effect enables monitoring of the blood flow in the vascular graft and identification of lesions in real time for up to three months. In male nonhuman primate cynomolgus monkeys, the electronic vascular conduit, with an integrated wireless signal transmission module, enables wireless and real-time hemodynamic monitoring and timely identification of thrombi. This electronic vascular conduit demonstrates potential as a treatment-monitoring platform, providing a sensitive and intuitive monitoring technique during the critical period after bypass surgery in patients with CAD and PAD.

Owing to the growing elderly population, the prevalence of vascular diseases has risen substantially^{1–3}. Arterial vascular grafts, particularly small-diameter grafts with internal diameters <6 mm, have important implications for coronary artery bypass graft (CABG) surgery, peripheral artery reconstruction, and arteriovenous fistula creation, but

suffer from problems related to slow endothelialization, which frequently results in platelet adhesion and initiation of the blood coagulation cascade^{4–7}, inducing thrombus formation and restenosis. According to clinical data, 10–15% of patients suffer from early graft dysfunction within 30 days after CABG surgery. Moreover, there is a

¹Beijing Institute of Nanoenergy and Nanosystems, Chinese Academy of Sciences, Beijing, China. ²School of Nanoscience and Engineering, University of Chinese Academy of Sciences, Beijing, China. ³School of Integrated Circuits and Electronics, Beijing Institute of Technology, Beijing, China. ⁴Department of Oral Surgery, Shanghai Ninth People's Hospital, Shanghai Jiao Tong University School of Medicine, Shanghai, China. ⁵Yonsei Frontier Lab, Yonsei University, Seoul, Republic of Korea. ⁶These authors contributed equally: Zhirong Liu, Chuyu Tang, Nannan Han.  e-mail: zhong.wang@mse.gatech.edu; zouduohongyy@163.com; lilinlin@binn.cas.cn

lifelong risk of blockage after surgery, especially for patients with underlying conditions such as hypertension, hyperlipidemia, and diabetes^{5–11}. There are multiple options for secondary revascularization, including guideline-directed medical treatment, percutaneous coronary intervention (PCI) and repeat CABG surgery; decision-making should be performed on a case-by-case basis¹². Generally, medical therapy can be a reasonable intervention for nonobstructive or intermediate lesions (30–60% diameter stenosis)^{13,14}. As the lesion progresses, PCI is commonly performed for secondary revascularization of dysfunctional grafts, and repeat CABG surgery, with high operative risk and possible peri-procedural complications, may even be required^{15–20}. We anticipate that timely and sensitive identification of abnormalities at the implant site during the early stage can enable less invasive and dangerous interventions for stopping progression^{21,22}.

In the clinic, hemodynamic evaluation is fundamental and indispensable for assessing the physiological status after graft transplantation and is commonly conducted using Doppler ultrasound, magnetic resonance imaging (MRI), and angiography^{23,24}. However, these methods require specialized equipment and skilled operators and might induce mechanical compression of local blood vessels, which is unsuitable for long-term continuous monitoring²⁵. Additionally, discharged patients are typically examined after ischemic symptoms recur, leading to delayed intervention and potentially necessitating a second surgery. In recent years, there have been advancements in the development of miniaturized and implantable hemodynamic monitoring electronics^{26,27}. These devices enable real-time monitoring based on the Doppler effect^{28,29}, photoplethysmography (PPG)^{30,31}, thermal analysis³² and electromechanical coupling effects^{22,33–35}. Nevertheless, these later-introduced sensors encounter issues such as mechanical mismatch and poor compatibility, increasing the risk of thrombosis and impeding in situ monitoring^{33,36}. Achieving long-term and in situ monitoring of hemadostenosis and blood flow signals remains a considerable challenge, particularly in the complex physiological environment following surgery. Due to the pervasive nature of triboelectric phenomena, triboelectric sensors provide a broader selection of materials, expecting to give consideration to biocompatibility, flexibility and heightened sensitivity³⁷.

We present an electronic vascular conduit with an integrate flexible triboelectric sensor wrapped around the bionic vascular graft, allowing in situ and real-time hemodynamic monitoring following vascular replacement. Considering the anisotropic properties of natural arteries, we fabricated a mechanically and structurally matching vascular graft that can expedite vascular endothelialization and achieve a high patency rate in a rabbit carotid artery transplantation model over a 3-month transplantation period. The flexible pressure sensor, bioinspired by arterial baroreceptors and encompassing the graft, exploits the triboelectric effect for sensing and possesses high adaptability. Its three-dimensional (3D) friction characteristic enables the sensitive perception of weak blood flow signals, allowing real-time and in situ monitoring of the physiological condition of vascular grafts, including restenosis and thrombus. These captured hemodynamic signals, extracted from the electrical output of the sensor, are wirelessly transmitted through a Bluetooth low-energy (BLE) module and visualized in real time on a customized cell phone application (app) at predefined times and intervals. The system has demonstrated over 3 months of real-time and wireless hemodynamic monitoring, reflecting artery repair and thrombosis and demonstrating potential for guiding decision-making. Our electronic vascular conduit represents a comprehensive proof-of-concept platform with promise for the treatment and concurrent postoperative evaluation of patients with CAD and PAD.

Results

Design concept of the electronic vascular conduit

Following bypass surgery or other microsurgical anastomosis, inflammation or thrombosis often leads to graft failure^{6,38}. To address

this issue, we designed an electronic vascular conduit that not only facilitates arterial reconstruction but also enables continuous wireless monitoring of in situ hemodynamics postimplantation, allowing early detection of lesions and timely intervention. The conduit comprises three main parts: i) an inner biomimetic double-layered artificial graft created by electrospinning; ii) a flexible triboelectric sensor encompassing the graft for real-time and in situ hemodynamic monitoring; and iii) a signal-processing circuit and BLE transmission module interconnected via a flexible printed circuit board (PCB) for wireless signal transmission (Fig. 1, Supplementary Fig. 1).

The artificial vascular graft features a double-layered structure, with the inner layer consisting of longitudinally aligned polycaprolactone nanofibers (PCL NFs), which mitigate blood flow resistance and promote host intimal endothelial cell (EC) migration from the anastomotic site toward the graft, thereby accelerating vascular endothelialization and diminishing the risk of postoperative thrombosis. The outer layer of the graft consists of anisotropic thermoplastic polyurethane nanofibers (TPU NFs) with mechanical properties comparable to those of native arteries; these fibers impart high tensile strength and resilience, enabling the graft to withstand surgical suturing and cardiac cycles.

The flexible sensor is integrated by seamlessly wrapping around the vascular graft. The sensor works based on the triboelectric effect between the polypyrrole (PPy) and polydimethylsiloxane (PDMS) films, which have complementary nanowire array structures to improve electromechanical coupling. During systole, compression of the sensor by the arterial wall brings the two triboelectric layers into contact, resulting in the transfer of electrons from the PPy surface to the PDMS surface due to the overlap of electron clouds. As diastole occurs, the distance between the charged triboelectric layers gradually increases, generating a potential difference between the two electrodes through electrostatic induction (Supplementary Fig. 2 and Movie 1). The complementary surface nanostructures of the triboelectric layers enhance the actual friction area, improving the electromechanical conversion performance of the sensor. This allows the sensor to detect pulse waves through monitoring periodic voltage changes. Once hemadostenosis occurs and a thrombus forms, the signal amplitude noticeably changes, accompanied by a tendency toward waveform deterioration. The flexible BLE transmission module is positioned between the adipose and dermis layers near the surgical site, and the customized software controls the timing and duration of wireless measurements and enables real-time display and storage of time-series blood flow data. For bypass graft surgery, this electronic vascular conduit enables timely monitoring of and early warning for vascular restenosis.

Fabrication and characterization of the electronic vascular conduit

Following reconstructive surgery, vascular implantation may fail due to secondary thrombosis, generally without evident premonitory symptoms. To address this issue, we integrated a self-powered pressure sensor around the vascular graft to enable real-time monitoring of hemodynamics following bypass surgery (Fig. 2a). And its dimensions (size, length, thickness) can be customized for applications in various anatomical sites or vascular graft configurations (Supplementary Fig. 3). First, considering the endothelialization mechanisms of the native artery, we fabricated a vascular graft with a porous structure and tunica intima topography akin to those of native tissue^{39–41}. Cross-sectional imaging of the vascular graft revealed a double-layered wall (300 μm in thickness, 2 mm in inner diameter) composed of a densely compacted and porous nanofibrous network, which ensures unhindered blood flow without posttransplantation leakage (Fig. 2b). The inner layer of PCL NFs was arranged in an orderly manner along the axial direction of blood flow (Fig. 2c, Supplementary Fig. 4), mimicking the structure of the tunica intima in native arteries. The simulation

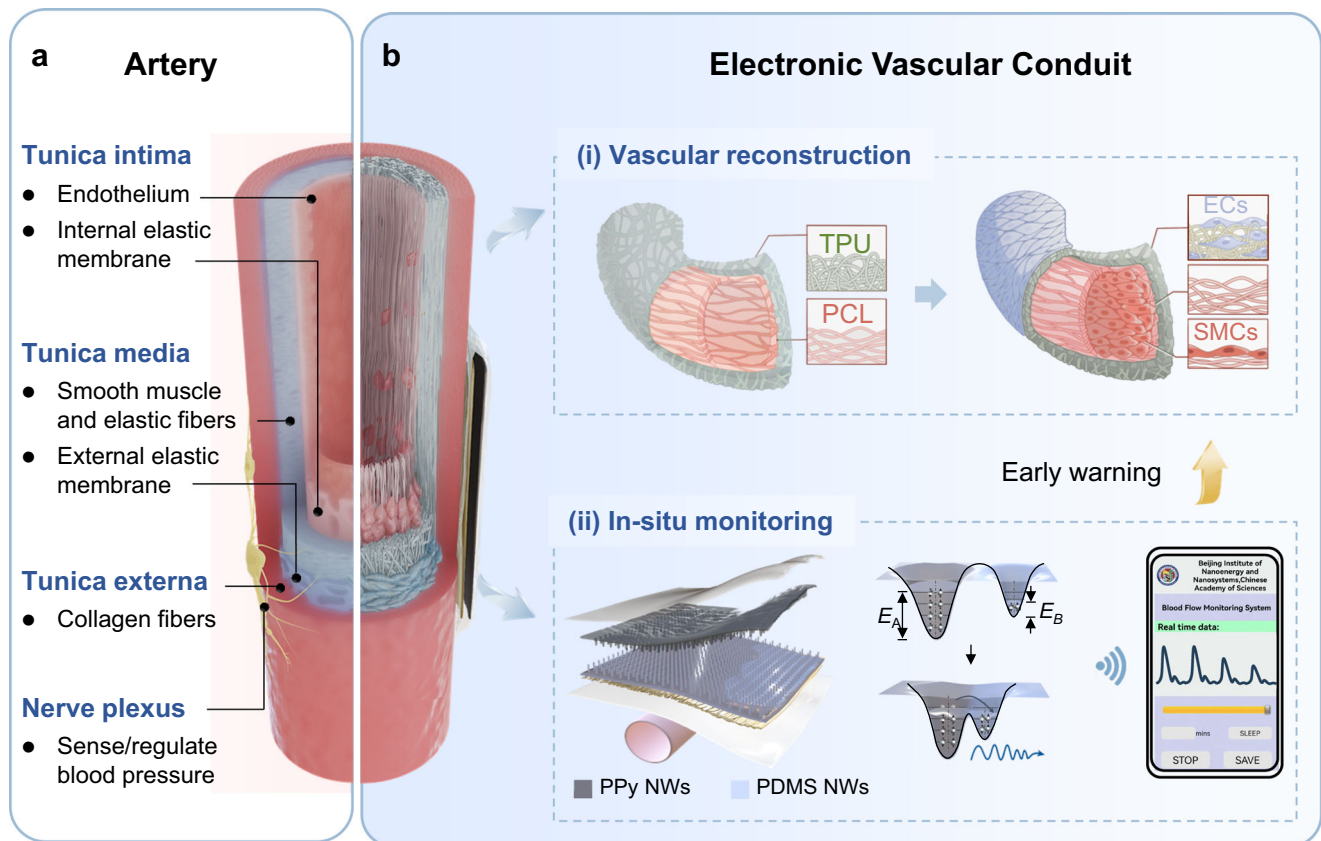


Fig. 1 | Overview of the native artery and electronic vascular conduit. **a** The native artery is composed of the intima, media and externa, endowing the artery with excellent mechanical properties and hemostasis-thrombus balance ability. The nerve plexus encompasses the artery to sense and regulate blood pressure. **b** Our electronic vascular conduit comprises i) a biomimetic artificial graft designed for

arterial reconstruction and ii) an integrated triboelectric sensor for real-time and in situ hemodynamic monitoring. **b-ii** illustrates the triboelectric sensor and its electron cloud and potential energy well model for electricity generation. E_A and E_B represent the occupied energy levels of electrons.

results demonstrated that blood flow is faster and steadier in the graft with longitudinally aligned nanofibers parallel to the blood flow direction, without noticeable abrupt changes; conversely, intersections on the surface of random nanofibers would cause disturbed blood flow and a slight decrease in blood flow velocity on the inner surface of blood vessels (Fig. 2d, Supplementary Fig. 5). Additionally, the elastic TPU NFs with exceptional mechanical stability was selected as the outer layer to provide sufficient tensile strength and suitable recoil capability during continuous contraction and relaxation (Fig. 2c, Supplementary Fig. 6).

A mechanically matched and conformable pressure sensor, bioinspired by arterial baroreceptors, was designed to encompass the graft for in situ hemodynamic monitoring based on the triboelectric effect. The triboelectric sensor utilized the PPy film as both the triboelectric layer and the electrode, as well as a PDMS film as another triboelectric layer, with an attached Au nanofibrous electrode (Au NFs) on its backside (Fig. 2a). These functional layers were encapsulated by a biocompatible PU/parylene-C film, preventing signal attenuation due to bodily fluids. By introducing complementary nanowire array structures (NWs) onto the friction layers (as shown in Fig. 2e, f and Supplementary Figs. 7, 8), the surface charge density and friction area can be enhanced, thereby improving the electromechanical conversion performance of the sensor. The uneven structure of the PPy film creates an air microspacer between the friction layers, ensuring continuous contact-separation cycles during periodic pulse waves. The electrode with aligned Au NFs exhibited exceptional electrical stability when the stretching direction was perpendicular to the extension direction of the nanofibers (Fig. 2g, k and Supplementary Fig. 9). In the

final electronic vascular conduit, the nanofiber direction of the electrode was aligned with the axial direction of the artificial graft, ensuring stable resistance during periodic expansion and contraction of the graft. Then, the above functional layers were encapsulated by the biocompatible PU/parylene-C film to make the sensor waterproof and anti-fouling (Supplementary Fig. 10)^{42,43}. Consequently, the triboelectric effect between the friction layers enables the conversion of weak mechanical signals on the arterial surface into electrical outputs for blood flow monitoring.

Rapid endothelialization of the graft can substantially reduce blood clot formation and promote the maintenance of vascular tone, consequently mitigating early thrombosis risk^{44–46}. Focal adhesions (FAs), transmembrane connections between the extracellular matrix and the actin cytoskeleton, participate in key cell processes such as cell migration and wound healing^{47–49}. After human umbilical vein endothelial cells (HUVECs) were seeded on the PCL NFs and cultured for 48 h, we observed numerous mature FAs along the cell edges (Fig. 2h). Moreover, FAs in cells on aligned PCL (a-PCL) exhibited a preference for alignment with the direction of NF extension and cell spreading, whereas FAs in cells on random PCL (r-PCL) displayed a random orientation (Supplementary Figs. 11–13). In the cell migration experiment (Fig. 2i, j), the migration distance of cells parallel to the aligned NFs (a-PCL/p, 483.4 μm) was significantly greater than that of cells perpendicular to the aligned NFs (a-PCL/v, 143.7 μm) and cells on r-PCL (252.6 μm). Besides, PCL NFs exhibit good blood compatibility and effectively inhibit platelet deposition (Supplementary Fig. 14). These results indicated that axially ordered NFs can guide the attachment and

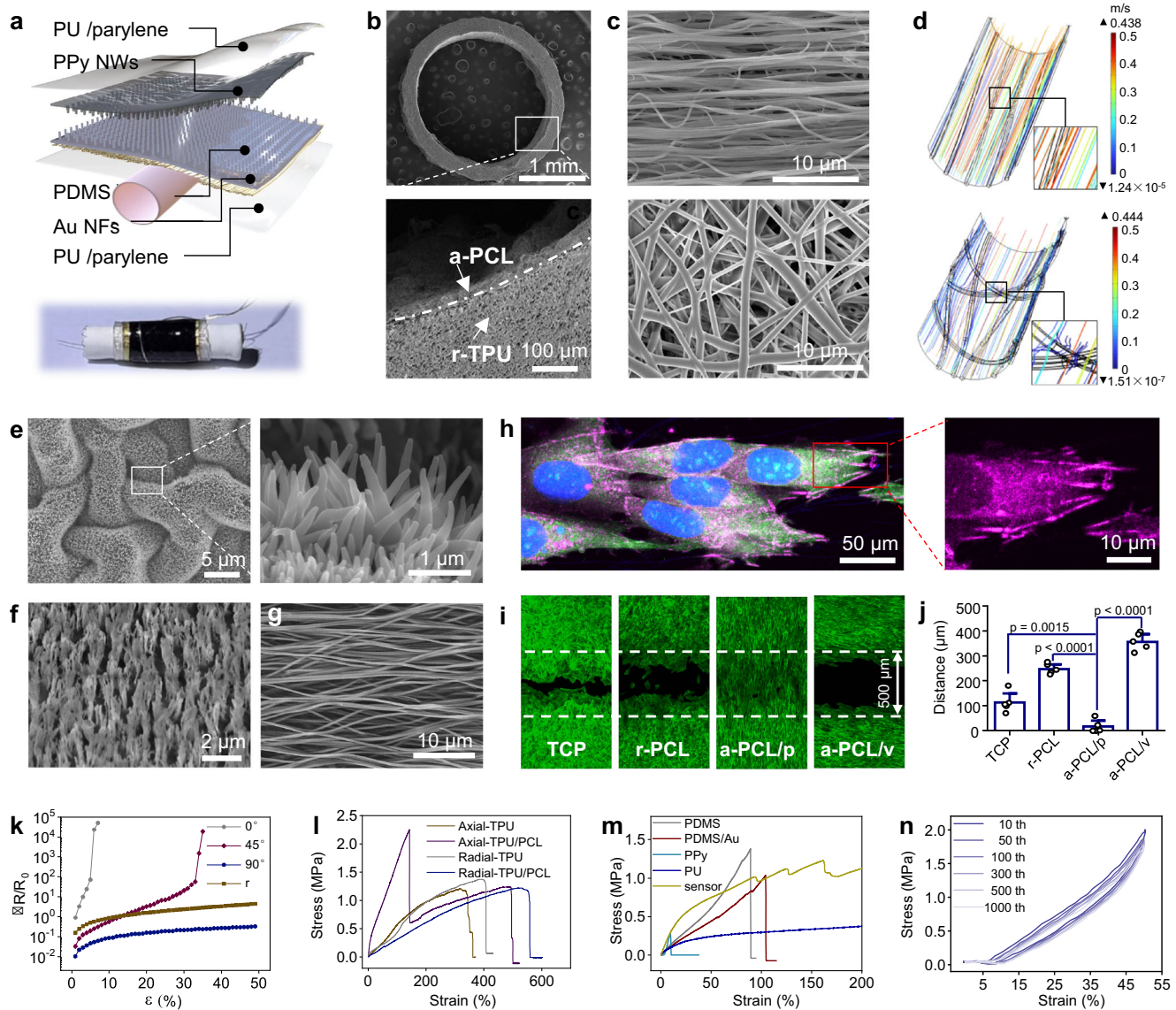


Fig. 2 | Characterization of the electronic vascular conduit. **a** The diagram and photograph of the electronic vascular conduit. **b** Cross-sectional scanning electron microscopy (SEM) images showing the double-layered, dense, fibrous structure of the graft wall. **c** SEM images of a-PCL (top) and r-TPU (bottom). **d** Numerical simulation of blood flow velocity on the axially ordered fibrous intima (top) and random fibrous intima (bottom). The blood flow was faster and steadier in the graft with axially ordered fibrous intima. SEM images of the (e) PPy and (f) PDMS films with nanowire array structures and (g) aligned Au NF electrodes. **h** Fluorescence microscopy images of HUVECs cultured on a-PCL and r-PCL for 48 h. F-actin was stained green, vinculin was stained magenta, and nuclei were stained blue. **i** Representative images of HUVEC migration in the scratch healing assay (width of

500 μm) for different samples after 24 h. **j** Statistical analysis of the scratch width in (i). Data are presented as mean values \pm SD, $n = 5$ independent experiments, one-tailed Student's *t*-test. **k** $\Delta R/R_0$ versus tensile strain for aligned Au NF electrodes under stretching in different directions and random Au NF electrodes. Representative stress–strain curves of (l) vascular grafts in the axial and radial directions and (m) each functional layer of the vascular sensor. **n** Stress–strain curves of the electronic vascular conduit after different numbers of cycles. In **b**, **c**, **e–h**, the experiments were repeated independently three times with similar results, and a representative result is shown for each. Source data are provided as a Source Data file.

directional migration of endothelial cells, expediting rapid endothelialization and vascular repair.

The mechanical compatibility between autologous blood vessels and vascular grafts also plays a key role in successful vascular repair and long-term patency following implantation^{40,50}. The stress–strain curves revealed favorable radial and axial elasticity of the electrospun tubular grafts (Fig. 2l), akin to the elastic modulus of healthy blood vessels, which typically ranges from 0.5 to 5 MPa. The sensor exhibited analogous elasticity (~ 2.3 MPa; Fig. 2m), ensuring that it did not impose mechanical constraints on the wrapped vascular graft. Additionally, both the vascular graft and the electronic vascular conduit exhibited high mechanical stability and consistently withstood applied stress

loading and unloading with minimal hysteresis (Fig. 2n, Supplementary Fig. 6). The elongation rate at the point of rupture for the tubular grafts surpassed 400%, representing a 1.5-fold increase compared with that of native vessels (Supplementary Fig. 15)⁵¹. Moreover, the electrospun grafts exhibited a high suture retention strength of approximately 2.95 N, indicating their suitability for surgical suturing. These results indicated that the candidate vascular graft had good biocompatibility and mechanical properties.

In vitro validation of the hemodynamic monitoring capabilities

Vascular electronics work on the basis of the triboelectric effect. With alternating contraction and diastole of the heart, blood flows

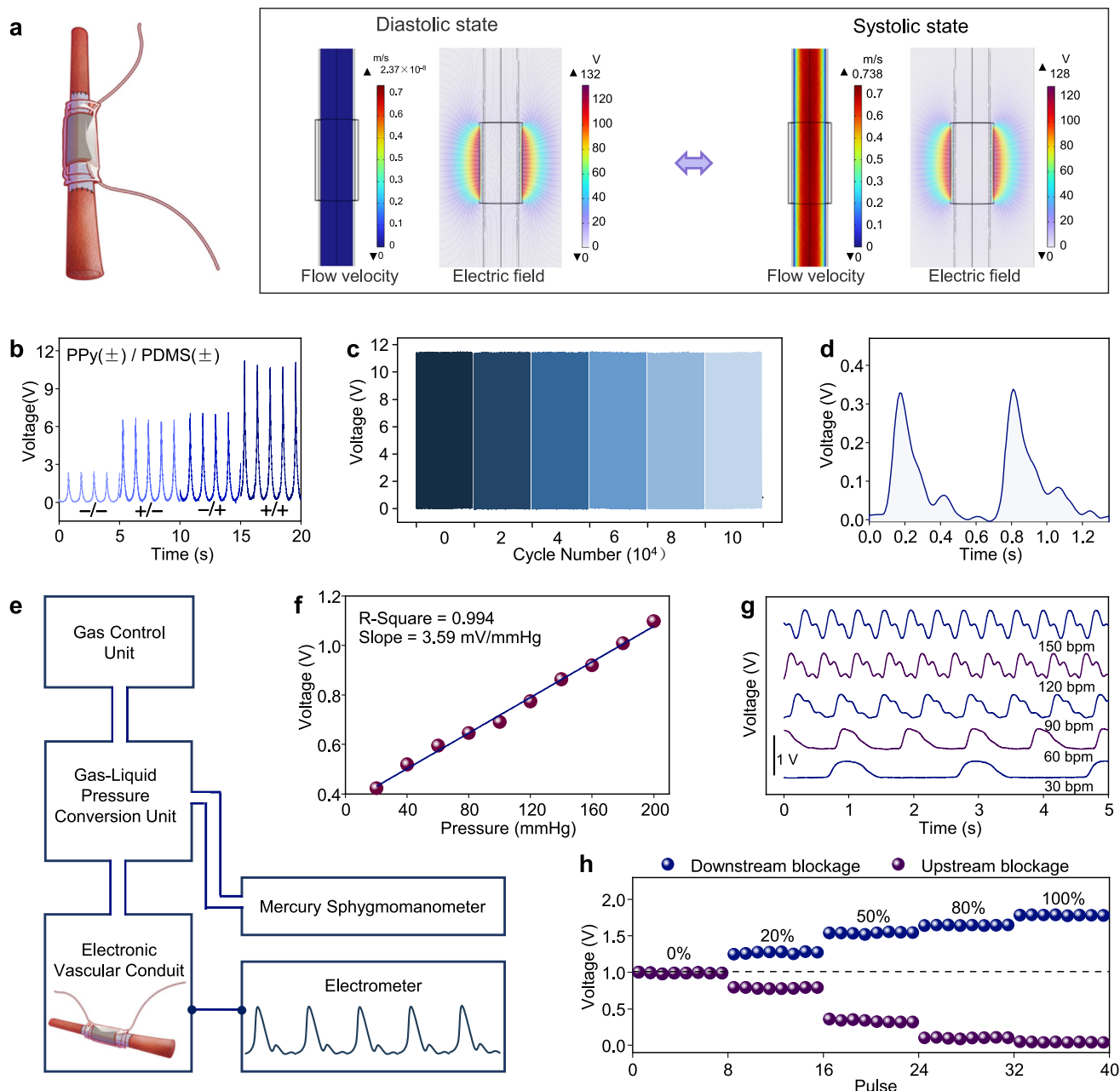


Fig. 3 | In vitro validation of the hemodynamic monitoring capabilities.

a Illustration and working principle of the electronic vascular conduit for hemodynamic monitoring. Vascular electronics work based on the triboelectric effect and electrostatic induction. During alternation of the diastolic and systolic states, the two friction layers contact and separate repeatedly, thus generating periodic electrical signals. **b** Output voltage of the sensor with different functional layers under a force of 1 N; +/- indicates films with/without the NW array structure. **c** Long-

term stability tests of the sensor (1 N, 1 Hz). **d**, Output voltage of the sensor for wearable pulse wave monitoring. **e** Schematic diagram of the in vitro blood pressure simulation and testing system. The system is regulated by an air pump and obtains measurements in real time using a commercial mercury sphygmomanometer. **f** Linear fit of the internal pressure and output voltage. **g** Output voltage of the sensor at different frequencies. **h** Output voltage of the sensor in the case of upstream or downstream blockage. Source data are provided as a Source Data file.

throughout the arterial vasculature in the form of pulse waves and is sensed by vascular electronics in the form of pressure waves. To simulate the working mechanism of vascular electronics, we fully coupled the flow velocity, pressure, and displacement with an electrostatic field to simulate the output of the sensor during the pulsation process. During ventricular systole, the sudden expansion of the artery brings the two triboelectric layers into contact, resulting in the generation of triboelectric charges. With the advent of diastole, vasoconstriction leads to the separation of triboelectric layers, thus generating induced charges on the electrodes (Fig. 3a, Supplementary

Fig. 2 and Movie 1). Through optimization of both morphology and electrical properties, the sensor demonstrated good durability and maintained a stable output voltage after more than 10,000 cycles of mechanical stimulation (Fig. 3b, c). When attached to the human neck, the sensor proved to be sensitive for monitoring the pulse wave of the carotid artery (Fig. 3d).

We initially evaluated the blood flow monitoring capability of the electronic vascular conduit using an in vitro model that replicates the pulsatile behavior of an artery (Fig. 3e). After gradually increasing the driving pressure from 20 to 200 mmHg at a frequency of 1 Hz, the

output voltage of the sensor displayed a corresponding increase, demonstrating a sensitivity of $3.59 \text{ mV mmHg}^{-1}$ and good linearity ($R^2 = 0.994$; Fig. 3f and Supplementary Fig. 16). Furthermore, the sensor exhibited a synchronous frequency response (Fig. 3g).

Subsequently, we assessed its ability to detect hemadostenosis and thrombosis using an *in vitro* occlusion model in which tension was applied to the artificial blood vessel through sutures. In cases where occlusions occurred upstream of the sensor, the output voltage gradually weakened as the blood flow volume in the artery at the sensor site decreased, and the signal nearly disappeared when the vessel was completely blocked. Conversely, when the downstream node was occluded, the output signal became stronger as the degree of blockage increased (Fig. 3h, Supplementary Fig. 17 and Movie 2). This phenomenon was attributed to the elevated pressure caused by a reduced vascular lumen volume and disturbed flow resulting from sudden stenosis. These results indicated that the electronic vascular conduit possesses the capability to monitor the location and progression of arterial embolism, offering valuable insights for postoperative monitoring.

Validation of the hemodynamic monitoring capabilities in rabbits

We proceeded to validate the *in vivo* hemodynamic monitoring capabilities of the electronic vascular conduit by surgically replacing the isometric left carotid artery in New Zealand rabbits through end-to-end anastomosis. Following transplantation, an electrometer connected to the triboelectric sensor recorded pulse waves at a frequency of 240.64 beats per minute (bpm) (Fig. 4a–c and Supplementary Movie 3). Respiratory motions were also evident in the waveform and were distinguishable from the pulse waves by notable differences in frequency and amplitude.

When we administered adrenaline (AD) as a receptor stimulant to modulate blood pressure, the sensor's output voltage exhibited a 1.15-fold increase (Fig. 4d, e). Based on the output frequency, the dispersion of heart rate values increased, with heart rate variability (HRV) shifting from 0.159 to 0.169. Over time, each parameter gradually returned to its initial value, suggesting recovery from the drug's influence. These results demonstrated that the electronic vascular conduit promptly and accurately reflected dynamic changes in hemodynamic parameters, enabling effective postoperative evaluation.

To demonstrate the capability of the electronic vascular conduit to monitor vascular stenosis following bypass surgery, we constructed occlusions via sequential compression and release of the proximal and distal ends of the vascular graft. Applying sutures to the proximal artery resulted in gradual stenosis. This was reflected by a decrease in the sensor's output voltage, with the relative intensity dropping from 1 to 0.595. Blood flow was restored upon loosening the suture, which was also reflected by the sensor in real time (Fig. 4f, h). In the case of distal artery occlusion, the signal amplitude noticeably increased from 1 to 1.975 due to disturbed flow caused by abrupt stenosis (Fig. 4g, i).

For a more realistic simulation of postoperative vascular restenosis, we utilized an electronic vascular conduit lacking an intima for vascular replacement of the isometric left carotid artery in New Zealand rabbits, by which the thrombosis forming and receding can be regulated by heparin. To facilitate long-term postoperative monitoring, we employed a BLE transmission module powered by a wireless charging module to achieve wireless hemodynamic monitoring and verified its long-term reliability for up to 3 months (Supplementary Figs. 18, 19 and Movies 4, 5). Anticoagulation treatment was suspended on the 30th day following surgery to induce an acute thrombosis. As a result, the output of the electronic vascular conduit decreased obviously. Color Doppler ultrasound results displayed that there was obvious abnormal blood flow in the artificial blood vessel, suggesting vascular stenosis was in progression (Fig. 4j). Subsequently, we re-

introduced heparin anticoagulation therapy, and observed that the output of artificial electronic blood vessels gradually recovered, consistent with the Doppler ultrasound results. These results demonstrated the stability and reliability of the electronic vascular conduit for long-term postoperative blood flow monitoring.

Tissue adaptability of the electronic vascular conduit

Currently, implantable electronics often face issues, including mechanical mismatch and poor compatibility, thereby increasing the risk of thrombosis and impeding *in situ* monitoring. To verify the influence of the integrated pressure sensor on the repair effect of our vascular graft, we investigated the long-term patency and endothelialization of the electronic vascular conduit by surgically replacing the isometric left carotid artery in New Zealand rabbits (Fig. 5a). At 3 months postsurgery, Doppler ultrasound imaging confirmed uninterrupted blood flow through both the electronic vascular conduit and native artery, with no indication of hemorrhage or aneurysm-like distension at the suture site (Fig. 5b).

We retrieved the grafts at 3 months postimplantation for overall assessment. Similar to the vascular grafts, the electronic vascular conduits were covered by remodeled tissues, and the lumen surface appeared smooth without any signs of thrombosis (Fig. 5c). Besides, the triboelectric sensor maintained close contact with the artificial graft, further affirming the long-term structural stability of the integrated electronic vascular conduit. Hematoxylin-eosin (H&E)-stained transverse tissue slices after a 3-month repair period revealed the presence of smooth and continuous tissue layers covering the graft lumen, resembling the tissue structure in the native vessel. We employed platelet endothelial cell adhesion molecule-1 (CD31) and alpha smooth muscle actin (α -SMA) as markers for the regeneration of functional endothelial cells and smooth muscle cells, respectively. As shown in Fig. 5d, the graft lumen was completely enveloped by a CD31⁺ endothelial cell layer for both the vascular grafts and the electronic vascular conduits, with a thickness of 2.6–2.8 μm and a coverage rate greater than 88% (Fig. 5e–g). An α -SMA⁺ contractile smooth muscle cell (SMC) layer was clearly observed exterior to the intima. Notably, the endothelial cell layer and smooth muscle layer exhibited tight adhesion, closely resembling the architecture of native vessels (Supplementary Figs. 20 and 21). SEM images further confirmed that the tunica intima was covered by endothelial cells that elongated along the direction of blood flow with a characteristic cobblestone-like morphology (Fig. 5h). No thrombosis or intimal hyperplasia was found. Besides, the surrounding tissue (connective tissue, nerve and muscle) and major organs (heart, liver, spleen, lung and kidney) appeared structurally normal, without obvious inflammation (Supplementary Figs. 22 and 23). On the basis of the above results, the integrated electronic vascular conduit exhibited reparative performance comparable to that of the vascular graft, indicating that the presence of the encapsulating sensor did not hinder blood vessel repair while monitoring blood flow *in situ*.

Wireless hemodynamic monitoring and identification of thrombi in cynomolgus monkeys

To facilitate postoperative management, we utilized a BLE transmission module with timing function powered by a lithium-ion battery to achieve wireless hemodynamic monitoring and verified its reliability in nonhuman primate cynomolgus monkeys. The block diagram in Fig. 6a illustrates the electrical architecture of the wireless monitoring module, which includes initial blood flow signal acquisition, baseline adjustment, signal amplification, low-pass filtering, and wireless transmission to a customized cell phone app. The app allows the user to configure the timing and duration of wireless measurements and signal transmission.

We surgically replaced both the unilateral carotid artery and the femoral artery in cynomolgus monkeys with an electronic

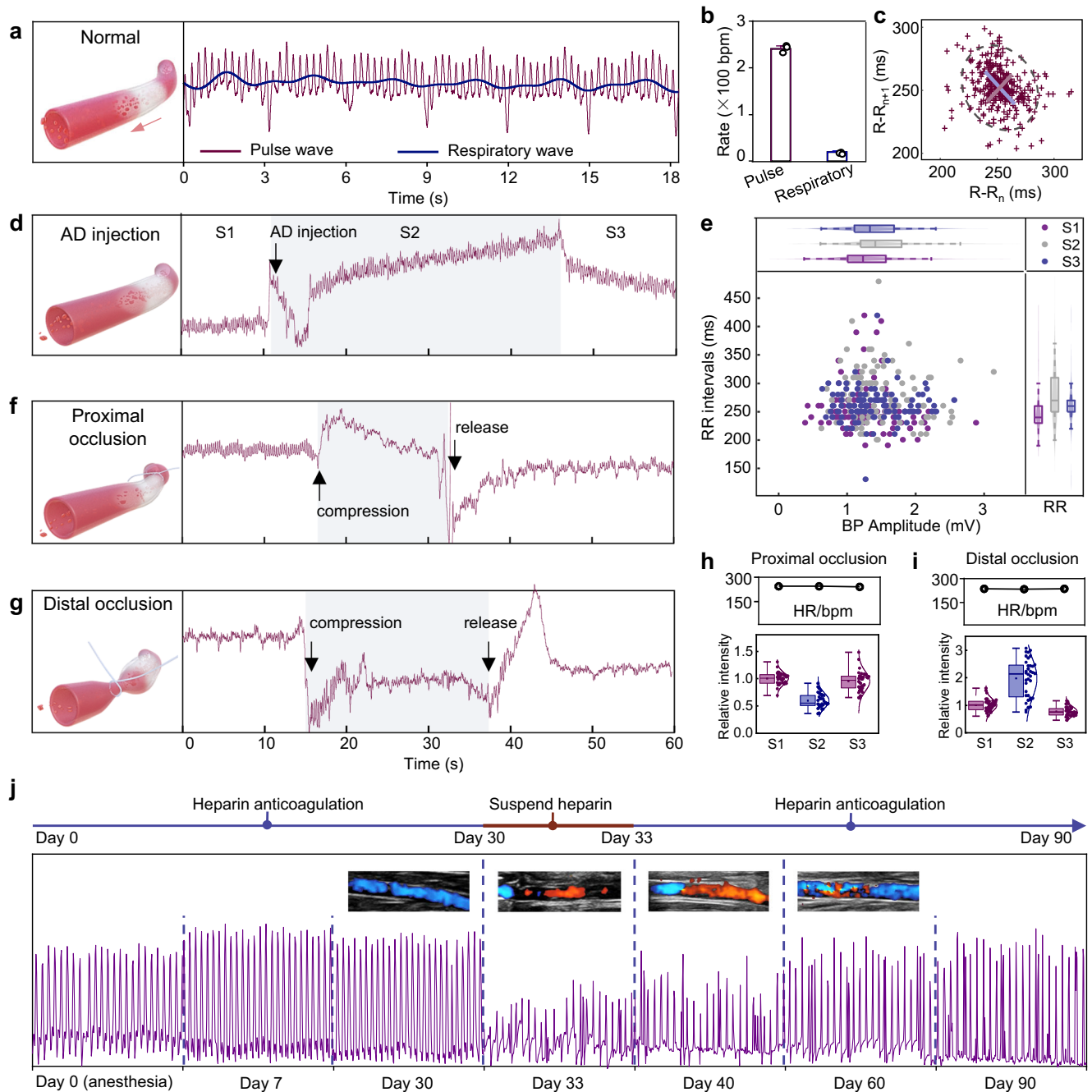


Fig. 4 | Real-time hemodynamic monitoring in rabbits. **a** Pulse and respiratory waves under anesthesia. **b** Statistical analysis of heart rate and respiratory rate. Data are presented as mean values \pm SD, $n = 3$ independent experiments. **c** Poincaré plots of the heartbeat interval (RR interval) under anesthesia. **d** Pulse waves after adrenaline injection. S1, S2, and S3 represent three different stages. **e** Scatter plot of pulse wave amplitude (BP amplitude) versus RR interval, where $n = 115$ (S1), 106 (S2) and 114 (S3) from 3 independent experiments. Box plots are defined as follows: the central line within the box represents the median (50th percentile), while the bounds of the box represent the 25th and 75th percentiles. The whiskers extend to

the minimum and maximum values. All individual data points are plotted. Pulse waves under **(f)** proximal and **(g)** distal occlusion and **(h, i)** corresponding amplitude statistics ($n = 30$ peaks from 3 independent experiments for each group). Box plots are defined as follows: the central line within the box represents the median (50th percentile), while the bounds of the box represent the 25th and 75th percentiles. The whiskers extend to the minimum and maximum values. All individual data points are plotted. **j** Monitoring results from the electronic vascular conduit and corresponding color Doppler ultrasound images. Source data are provided as a Source Data file.

vascular conduit (Fig. 6b and Supplementary Figs. 24–26). The PCB and a 140 mAh lithium-ion battery were embedded between the adipose and dermis layers near the surgical site (Fig. 6c). Figure 6d, e demonstrates the ability of the system to wirelessly monitor and transmit hemodynamic signals to the app. Regardless of the animal's status (asleep, awake, or active), the pulse wave signal was continuously and wirelessly displayed in real time in the

app (Supplementary Movies 6 and 7). During the postoperative anesthesia phase, the pulse waves remained stable, with a calculated pulse rate of 174 bpm. In comparison, in the awake state, the pulse rate increased to 252 bpm, and the amplitude of the pulse waves drastically increased (Fig. 6f–h). Over a period of 14 days during which the conduit was patent, the pulse wave signal exhibited high stability, as depicted in Fig. 6h, i.

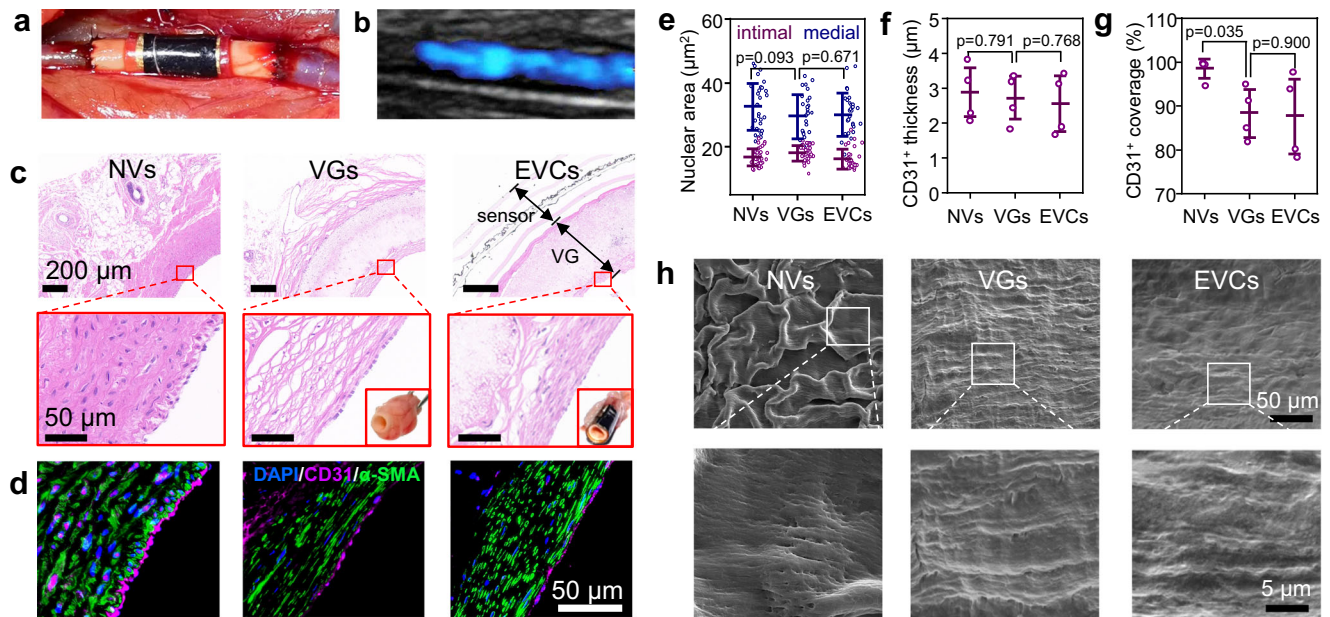


Fig. 5 | Tissue adaptability of the electronic vascular conduit. **a** End-to-end anastomosis for suturing of the electronic vascular conduit to the rabbit carotid artery. **b** Color Doppler ultrasound image of the electronic vascular conduit showing the continuity of blood flow. **c** H&E staining of cross-sections of different grafts after a 3-month repair period. Inset: optical images of the grafts. **d** Immunofluorescence staining of CD31⁺ and α -SMA⁺ cells in cross-sections of the graft showing a complete endothelial cell layer. Nuclei were stained with DAPI (blue). **e** Quantification of the nuclear area in the intimal and medial subsections of

the grafts. Data are presented as mean values \pm SD, $n = 30$ cells from 4 independent experiments, two-tailed Student's t -test. **f**, **g** Quantification of the CD31⁺ neointimal thickness and coverage rate. The values in **f** and **g** represent the mean values \pm SD, $n = 4$ independent experiments, two-tailed Student's t -test. **h** SEM images of the lumen surface of the grafts. The experiments were repeated independently four times with similar results, and a representative result is shown. NVs native vessels; VGs: vascular grafts; EVCs: electronic vascular conduits. Source data are provided as a Source Data file.

Following bypass surgery, the damaged intima activates the coagulation system, leading to increased blood coagulation and platelet aggregation on the rough surface of the damaged intima. Rejection and inflammation further accelerate thrombus formation, causing slowed or disturbed blood flow. Therefore, in the clinic, patients need to take anticoagulant drugs for life after bypass surgery to reduce platelet aggregation and blood viscosity. To investigate the ability of the electronic vascular conduit to sense vascular restenosis and thrombus, anticoagulation treatment was terminated on day 14 following surgery to induce acute thrombosis. The results recorded from the electronic vascular conduit are depicted in Fig. 6h. In contrast to the clear pulse wave during the first 14 days, the signal amplitude substantially decreased upon the cessation of anticoagulation treatment on day 15, and the signal nearly disappeared on day 16, accompanied by a tendency toward waveform deterioration. In addition, the pulse wave integrals reflected the deceleration of blood flow, indicating that a thrombus may have formed (Fig. 6i). To test our hypothesis, the grafts were retrieved for histological assessment. H&E-stained transverse tissue slices revealed that the lumen of the graft was filled with aggregated blood cells, which is representative of acute thrombus caused by an incomplete intima (Supplementary Fig. 27). Meanwhile, the sensor extracted after the animal experiments continued to function normally, retaining its sensitivity to subtle biomechanical signals (Supplementary Fig. 28). These results indicated that the electronic vascular system could be used for wireless and in situ monitoring of vascular restenosis and thrombus following surgical procedures. With the benefit of convenient and continuous data collection, this approach can assist in evaluating the repair and thrombosis process to guide clinical decision-making.

Discussion

Bypass graft surgery is used for the treatment of atheromatous blockages in a patient's coronary or peripheral arteries using bypass

grafts. Due to the inaccessibility of autologous grafts, the Food and Drug Administration (FDA) has granted approval for several synthetic vascular grafts, including expanded polytetrafluoroethylene (Teflon[®]) and polyethylene terephthalate (Dacron[®]) grafts⁵². These grafts have demonstrated efficacy as bypass conduits in patients with vascular stenosis or hemodialysis. However, until recently, graft patency has remained the Achilles' heel of bypass graft surgery⁵³. This is primarily due to issues such as foreign-body reactions, intimal hyperplasia, and a persistent risk of infection, all of which significantly increase the likelihood of acute thrombosis and vascular occlusion at the bypass site^{54,55}. Clinical research has revealed that early identification and treatment of vascular graft lesions can be achieved via less invasive procedures, thereby reducing the rate of graft transplantation failure. Therefore, the development of techniques for the timely and sensitive monitoring of vascular restenosis and progressive thrombus is highly desirable. In this study, we developed a comprehensive proof-of-concept electronic vascular conduit that is promising for the treatment and concurrent postoperative monitoring of patients with cardiovascular diseases. We investigated the potential application of this conduit in bypass graft surgery for real-time and wireless hemodynamic monitoring in rabbits and cynomolgus monkeys.

By integrating a highly sensitive triboelectric sensor around the bionic artificial graft, we can realize in situ and real-time monitoring of hemodynamics and timely identification of thrombosis in vascular grafts after bypass surgery. With respect to the cynomolgus monkey model, we confirmed that the system is capable of wirelessly transmitting hemodynamic signals following bypass surgery and facilitating timely identification of hemadostenosis and thrombosis. For bypass surgery in patients, the first postoperative week is recognized as a critical period that requires vigilant monitoring by healthcare professionals. During this time, physicians need to closely monitor the patient's condition and employ necessary interventions to prevent and manage any potential complications. Our electronic vascular system

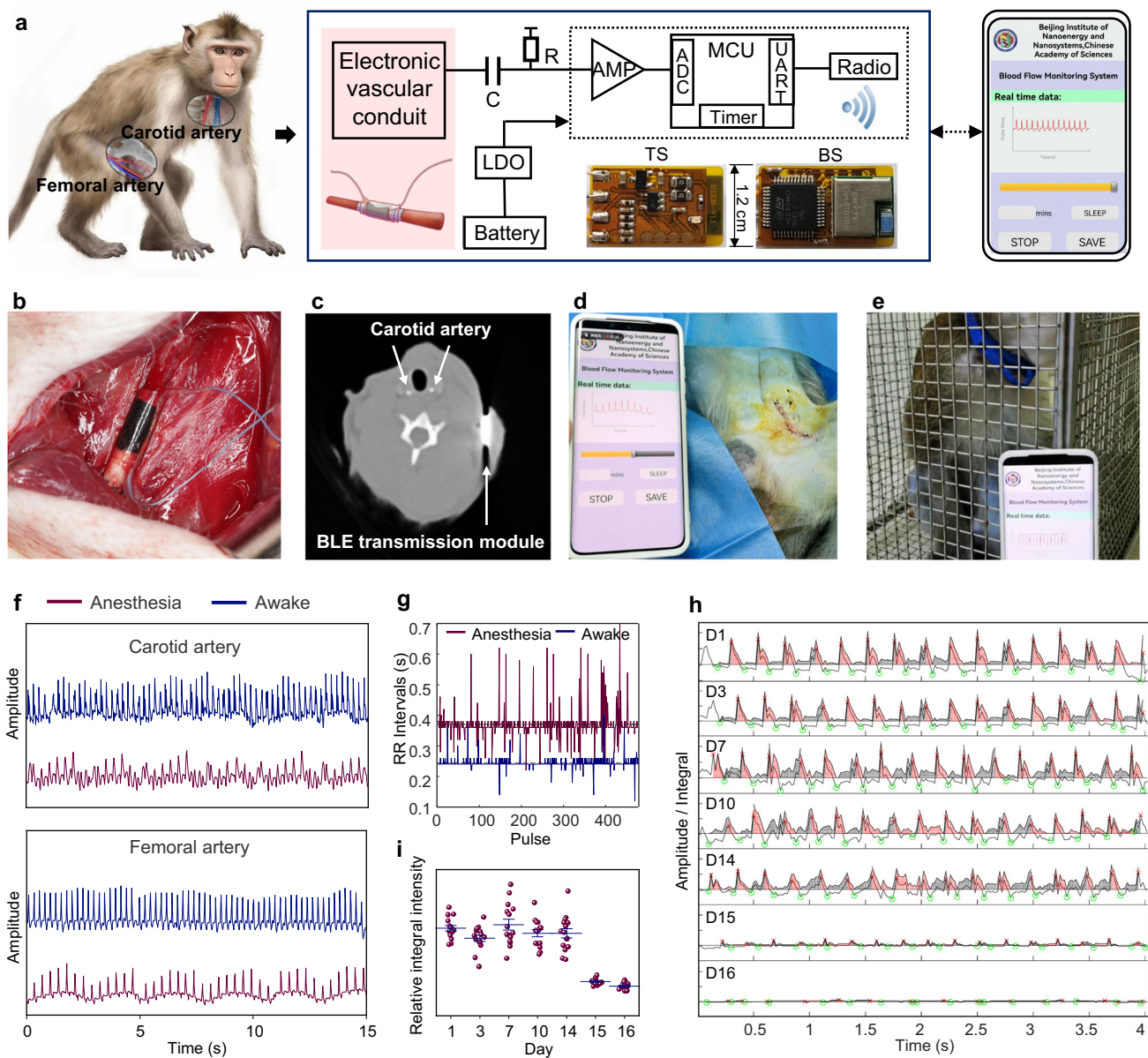


Fig. 6 | Real-time and wireless hemodynamic monitoring in cynomolgus monkeys. **a** Circuit and block diagram of the wireless transmission and control module. AMP amplifier, MCU micro control unit, ADC analog-to-digital conversion, UART universal asynchronous receiver/transmitter, LDO low-dropout regulator. Inset: optical photographs of the BLE module. TS top side; BS bottom side. **b** Optical images of the experimental setup for the cynomolgus monkey model. **c** CT image after implantation of the electronic vascular conduit. Real-time monitoring and display of pulse waves in the **(d)** anesthesia and **(e)** awake states after

surgery. **f** Pulse waves of the carotid artery and femoral artery in the anesthetized and awake states after surgery. **g** Statistical analysis of the heartbeat interval (RR interval). **h** Wireless monitoring of pulse waves after surgery. Anticoagulation treatment was terminated on day 14 (D14) to induce acute thrombosis. Gray: ascending limb of the pulse wave; red: descending limb of the pulse wave. **i** Relative integrals of pulse waves over different days. Data are presented as mean values \pm SD, $n = 15$ pulses from 3 independent experiments. Source data are provided as a Source Data file.

provides a convenient and intuitive solution for postoperative hemodynamic monitoring and identification of hemadostenosis and thrombosis and can assist in evaluating the progression of repair and warning signs of thrombosis.

In summary, we successfully developed an electronic vascular conduit and system inspired by native arteries and arterial baroreceptors. During the critical postoperative period following bypass graft surgery, the integrated triboelectric pressure sensor surrounding the bionic artificial graft enables real-time monitoring of the hemodynamic status at the implant site. This allows timely detection of any abnormalities, including vascular restenosis and thrombus formation, facilitating the adoption of less invasive treatment procedures and

reducing the risk of progressive thrombosis. In the future, we anticipate that by establishing direct connections and feedback loops among multiple functional modules, we will enable our conduit to overcome the limitations associated with artificial blood vessels in clinical applications.

Methods

Animals

Twelve New Zealand rabbits (male, 3–4 kg, ~6 months) were purchased from Experimental Animal Breeding Center, Beijing, for unilateral carotid artery replacement. All rabbits were individually housed in an animal room with controlled humidity of 40–70%, temperature of

22–26 °C, and a 12/12 light–dark cycle. Their diet includes SPF-grade maintenance chow, hay, and fresh vegetables. The cage provides toys to encourage natural behaviors and reduce stress. All animal handling procedures were in strict compliance with the Beijing Administration Rule of Laboratory Animals and the national standards Laboratory Animal Requirements of Environment and Housing Facilities (GB 14925-2001). The animal experiments were approved by the Committee on Ethics of Beijing Institute of Nanoenergy and Nanosystems (Approval Number: 2022A042).

Four adult cynomolgus monkeys (*Macaca fascicularis*, male, aged approximately 5 years, 4–6 kg) were purchased from Fangchenggang Changchun Biotechnology Development Co., Ltd, Guangxi. The monkeys were individually housed in an animal room with controlled humidity of 40–70%, temperature of 22–26 °C, and a 12/12 light–dark cycle. The monkeys were housed in stainless steel monkey cages. During the adaptation period, two monkeys were housed per cage (1600 mm × 1400 mm × 1640 mm); during the experimental period, each monkey were housed in a separate cage (800 mm × 700 mm × 820 mm). Their diet includes SPF-grade high-quality monkey chow, fresh fruits, vegetables, and sources of protein (such as nuts and legumes). The enclosure provides climbing structures, toys, and mirrors to promote natural behavior and alleviate stress. The animal experiments were conducted in PharmaLegacy Laboratories (Shanghai) Co., Ltd. (Approval Number: PL22-0871), which was certified by AAALAC (Association for Assessment and Accreditation of Laboratory Animal Care International). Animal experiments followed US National Institutes of Health regulations and were approved by the Institutional Animal Care and Use Committee (IACUC).

Preparation of PCL/TPU vascular grafts

PCL/TPU vascular grafts were fabricated by electrospinning. A mixture of dimethylformamide (DMF) and dichloromethane (3:1 by volume) was used as the solvent for TPU, with a concentration of 37.5 wt%. The PCL solution was prepared by dissolving 20 wt% PCL in 1,1,1,3,3,3-fluoro 2-propanol (HFIP). Then, the electrospinning solution was loaded into a plastic syringe equipped with a 21 G needle, and the flow rate was controlled at 1 mL h⁻¹. A constant voltage of 20 kV was applied between the needle and the metal collector, with a distance of 15 cm. For the random TPU tube, a stainless steel rod rotating at 200 rpm was used as the collector. Afterward, a receiving rod with a two-end electrode was used to collect axially-ordered PCL nanofibers under slow rotation. To improve hydrophilicity for tissue growth, the nanofiber tube was treated with oxygen plasma for 3 min. Finally, the inner and outer layers of the tube were reversed to obtain the PCL/TPU vascular graft. The morphology of the nanofibers and vascular grafts was evaluated by scanning electron microscopy (FEI Nova Nano SEM 450). The water contact angle was measured via contact angle measurements (XG-CAMBI, Xuanyi). A universal tensile testing machine (YLS71, Yuelian) was employed for the mechanical tests. The specimen dimensions were 15 mm in length and 10 cm in width. For the stress-strain curve tests, the stretching speed was maintained at 10 mm/min until the samples fractured. In the cyclic stability tests, the stretching frequency was set to 1 Hz, with a tensile elongation of 10%.

Fabrication and characterization of vascular electronics

Synthesis of PPy nanowires. PPy nanowires were synthesized via an electrochemical polymerization process. Five milliliters of pyrrole monomer (Py, Aladdin) was dissolved in 100 mL of NaClO₄ solution (0.3 mol L⁻¹). Electropolymerization was performed in a three-electrode electrochemical workstation (CHI 660F instruments), where conductive glass (ITO, 4 cm × 2 cm), Pt and Ag/AgCl were used as the working, counter and reference electrodes, respectively. Electropolymerization proceeded at a potential of 0.8 V for 300–500 s. Subsequently, a thin gold film was deposited on the PPy film via magnetron sputtering (50 W, 500 s), enabling the subsequent

synthesis of PPy nanowires via further electrochemical deposition. Specifically, 1 mM p-toluenesulfonic acid (p-TSA) was added to 51 mL of NaH₂PO₄ (0.2 mol L⁻¹) and 49 mL of Na₂HPO₄ (0.2 mol L⁻¹). After stirring until the mixture was dissolved, 1 mL of Py monomer was added. Then, electropolymerization was performed at a current density of 0.6 mA cm⁻² for 1.5–2 h, with PPy film-Au and Pt electrodes used as the working and counter electrodes, respectively.

Fabrication of PDMS nanowires. A PDMS film with a thickness of ~60 μm was obtained by spin coating and drying. Afterward, Au nanoparticles were sputtered onto the film to serve as a mask, facilitating the subsequent fabrication of PDMS nanowires through inductively coupled plasma (ICP) reactive-ion etching. The gas flow rates of Ar, O₂, and CF₄ were precisely adjusted to 15, 10 and 30 sccm, respectively, and the pressure was adjusted to 1–2 Pa. The power source for generating high-density plasma was 400 W, and the power source for accelerating plasma ions in the inductive coupling cavity was 100 W. The density and length of the nanowires were controlled by adjusting the mask density and the plasma etching time, respectively.

Fabrication of Au NF electrodes and PDMS nanowire-Au NFs. First, aligned PVA NFs were fabricated by electrospinning a 10 wt% PVA solution in water onto a parallel-plate electrode receiver at a flow rate of 0.5 mL h⁻¹ and a constant potential of 13 kV. Subsequently, a thin gold layer was deposited on the PVA NFs by magnetron sputtering (50 W, 200 s, PVD75 Kurt J. Lesker) to form a uniform core-shell coating. The PVA/Au core/shell NFs were placed on the water surface and then transferred to the backside of the PDMS substrate to obtain PDMS nanowire-Au NFs.

Assembly of the triboelectric sensor and integration of the electronic vascular conduit. The sensors based on the triboelectric effect include triboelectric layers, electrode layers, and encapsulation layers. Specifically, the PPy nanowire film acted as both an outer triboelectric layer and an electrode. PDMS nanowire-Au NFs were employed as the inner triboelectric layer and electrode. The surfaces with nanowire structures were placed opposite to each other. Then, the above functional layers were encapsulated by the biocompatible PU tape/parlylene-C film to make the sensor waterproof. Finally, we assembled the sensor on the vascular graft through the reserved interface on the medical PU tape. The mechanical properties of autologous blood vessel, the artificial graft and the sensor were matching, thereby minimizing the poor contact caused by mechanical mismatch during the periodic expansion and contraction of blood vessels.

In vitro measurement setup

A measurement setup was built to simulate blood flow in vitro and verify the ability of the sensor to monitor blood flow. The setup included a gas control unit, a gas–liquid pressure conversion unit connected to an electronic vascular conduit, an electrometer for recording the output of the sensor, and a standard medical mercury column pressure gauge for monitoring system pressure. The system pressure and frequency were controlled from 20–200 mmHg by the gas control unit, and the output voltage of the sensor was recorded and compared with the mercury column pressure gauge that served as a reference standard. An in vitro occlusion model was generated by applying tension to artificial blood vessels by suturing.

Cell viability and proliferation on the nanofibers

HUVECs were obtained from the American Type Culture Collection (CRL-1730) and cultured in high-glucose (4.5 g L⁻¹) Dulbecco's modified Eagle's medium (H-DMEM, Gibco) supplemented with 10% fetal bovine serum (FBS, Gibco) and 1% penicillin–streptomycin (Gibco) in a humidified atmosphere of 5% CO₂ at 37 °C. The nanofibers were sterilized with 70% ethanol and UV exposure, followed by three rinses with PBS. A cell suspension (2 × 10⁵ cells mL⁻¹) was then seeded onto the nanofibers in 24- or 48-well plates. After 48 h of culture, cell viability was evaluated using a live/dead cell imaging kit (Life Technologies).

Cell proliferation on the nanofibers was quantified using a Cell Counting Kit-8 (CCK-8; Dojindo Molecular Technology) assay at 1, 3 and 5 days of culture, according to the manufacturer's instructions.

Cell morphology

Immunofluorescence staining for F-actin, vinculin and nuclei was performed in HUVECs after 48 h of culture. Cells on the nanofibers were washed twice with PBS, fixed with 4% formaldehyde in PBS for 30 min, permeabilized with 0.1% Triton X-100 for 10 min, and blocked with 10% goat serum for 2 h. The cells were incubated with primary antibody (anti-vinculin, 1:200) at 4 °C overnight and then incubated with secondary antibody (Cy3-conjugated goat anti-mouse IgG, 1:200) at room temperature for 2 h. F-actin was stained with phalloidin-conjugated Alexa Fluor 488 (1:200) for 2 h, and then the cells were stained with 4' 6-diamidino-2-phenylindole (DAPI, 300 nM) for 15 min. After each step, the cells were washed with PBS three times. Finally, the samples were imaged with a Leica confocal microscope (Leica, SP8).

SEM was used to observe the morphology of the cells on the nanofibers. After culturing HUVECs for 48 h, the cells were washed twice with PBS and fixed with 2.5% glutaraldehyde overnight at 4 °C. Then, the cells were dehydrated gradually using a series of ethanol in water (30%, 50%, 70%, 80%, 90%, 95%, 98%, and 100%) two times. Finally, the samples were imaged via SEM after being sputter-coated with gold.

Hemolysis test

Red blood cells (RBCs) were obtained by centrifuging fresh New Zealand rabbit blood containing anticoagulant (132 g, 10 min). The whole blood was washed 5 times with PBS to completely remove the serum. The obtained RBCs were diluted 10-fold with PBS before the hemolysis test. Then, the diluted RBCs (0.1 mL) were mixed with 5 mL of PBS solution and incubated with different samples ($1 \times 1 \text{ cm}^2$) at 37 °C for 2 h. Equal numbers of RBCs mixed with Milli-Q water and normal saline were used as positive and negative controls, respectively. After incubation for 2 h, all suspensions were centrifuged, and the absorbance of the supernatant at 545 nm was measured. The hemolysis rate (HR) was calculated as follows:

$$\text{HR}(\%) = \frac{A_s - A_n}{A_p - A_n} \times 100\% \quad (1)$$

where A_s , A_p , and A_n are the absorbency of the experimental group, positive control and negative control, respectively.

Platelet adhesion test

Platelet-rich plasma (PRP) was obtained by centrifuging fresh New Zealand rabbit blood at 206 g for 10 min. Different samples ($1 \times 1 \text{ cm}^2$) were sterilized and placed in 24-well plates. Then, PRP (350 μL , well⁻¹) was added and incubated at 37 °C under gentle shaking for 3 h. Afterward, the samples were gently rinsed with PBS to remove unattached platelets. The number of adherent platelets was determined using an LDH release assay kit. To directly observe platelet adhesion, the samples were fixed in 4% paraformaldehyde, dehydrated in gradient ethanol and observed by SEM.

In situ replacement of the rabbit carotid artery

Twelve New Zealand rabbits (male, 3–4 kg, ~6 months) were randomly divided into 3 groups, control, vascular grafts and electronic vascular conduits, for unilateral carotid artery replacement. The grafts were sterilized and then soaked in heparin (70 U mL⁻¹) for approximately 4 h. Before the operation, heparin was injected intravenously into the ear margin of each rabbit. After anesthesia with pentobarbital sodium, a 10 mm segment of the left carotid artery was transected and replaced with a PCL/TPU or TPU vascular graft or electronic vascular conduit (2 mm in diameter, 10 mm in length) via an anastomosis procedure.

Heparin (20 U kg⁻¹) was injected intravenously for 2 weeks after the operation for anticoagulant therapy. Doppler ultrasound (Mindray, Vetus 5) was used to evaluate the function of the blood vessels every 2 weeks. The rabbits were euthanized by first anesthetizing, followed by intravenous administration of potassium chloride (75–150 mg kg⁻¹). Histopathological analysis of the vascular grafts and major organs (heart, liver, spleen, lungs, and kidneys) was then performed. The vascular grafts were evaluated by H&E staining, Masson's trichrome staining, immunofluorescence staining (for CD31 and α -SMA) and SEM observation at 3 months after surgery.

Wireless hemodynamic monitoring system

To facilitate postoperative management, we utilized a BLE transmission module conjugated with an electronic vascular conduit to achieve wireless hemodynamic monitoring. The system was powered by a lithium-ion battery or a wireless charging module. The PCB and battery were encapsulated together in a 3D-printed box made from either PLA or photopolymer resin. After sealing the box with glue, a parylene-C coating was applied to the surface via vacuum vapor deposition to enhance biocompatibility and waterproofing.

In vivo sensor function assessment in New Zealand rabbits

After the electronic vascular conduit was implanted to replace the isometric left carotid artery in New Zealand rabbits, the sensor was connected to an electrometer (Keithley 6514) to monitor the output voltage. Blood pressure and heart rate were regulated via intravenous injection of adrenaline ($10^{-6} \text{ mol L}^{-1}$) to verify the ability of the sensor to monitor hemodynamics in vivo. In addition, the proximal and distal ends of the artificial blood vessel were blocked sequentially via suture compression to verify its ability to monitor thrombosis.

Wireless hemodynamic monitoring in cynomolgus monkeys

The electronic vascular system was sterilized with glutaraldehyde. Four adult cynomolgus monkeys (male, 4–6 kg) were fasted for 12 h before the operation and anesthetized by an injection of Zoletil (1.5–5.0 mg kg⁻¹). The animals were intratracheally intubated and kept anesthetized with 2–5% isoflurane during surgery. Afterward, the carotid or femoral artery of each cynomolgus monkey was replaced with an electronic vascular conduit via an anastomosis procedure. The PCB and the lithium-ion battery were buried between the adipose layer and dermis layer near the operation site. After implantation, the pulse wave signal was displayed on the app interface in real time via a wireless signal transmission system. During the postoperative recovery period, cephalosporin (0.1 g kg⁻¹) and dexamethasone (1 mg kg⁻¹) were injected for anti-infection treatment, and heparin (20 U kg⁻¹) was injected for anticoagulation treatment. Tolfenamic acid (4 mg kg⁻¹, twice a day) was injected intramuscularly for three days after the surgery, and the condition of each animal was closely monitored. For postoperative blood flow monitoring, the cynomolgus monkeys were placed in transfer cages, and data were collected using a non-contact Bluetooth module at a distance. For animal euthanasia, we used the most humane methods in accordance with the recommendations of the Panel on Euthanasia of the American Veterinary Medical Association and the guidelines of the National Institutes of Health Guide for the Care and Use of Laboratory Animals. The animals were anesthetized via intramuscular injection of Zoletil (2–3 mg/kg), and once deep anesthesia was achieved, euthanasia was performed by a rapid intravenous injection of KCl (75–150 mg kg⁻¹).

Numerical simulation

Numerical simulations were performed using COMSOL 6.1 software. To evaluate the effect of intimal topography on blood flow features, we constructed different geometric models in which the surface fibers gradually changed from an axially ordered state to a disordered state. To avoid the impact of fiber volume on blood flow, the total volume of

the fibers was kept essentially the same. In all the models, a constant velocity (35 cm s^{-1}) was set as the inlet and outlet conditions. The initial flow direction was along the axial direction, and at the inlet (cross-section of the plate at $x = 0$), the velocity remained constant.

To illustrate the hemodynamic monitoring capability of the electronic vascular conduit, an arterial model was built using Neo-Hooke elasticity with an external diameter of 2 mm and an elastic modulus of 6 MPa. The analysis consists of two distinct but coupled procedures: first, a fluid-dynamics analysis including a calculation of the velocity field and pressure distribution in the blood (variable in time and in space); second, a mechanical analysis of the deformation of the tissue and artery. For fluid dynamics analysis, two pressure conditions were established with reference to statistical blood flow information for establishing the boundary conditions: 11208 Pa for inlet end and 11192 Pa for outlet end. Those pressure values are the mean values over a heart-beating cycle. For the time-dependent analysis, a simple trigonometric function is used for varying the pressure distribution over time (Fluid-Structure Interaction in a Network of Blood Vessels, <https://cn.comsol.com/model/fluid-structure-interaction-in-a-network-of-blood-vessels-660>):

$$f(t) = \begin{cases} \sin \pi t & 0 \leq t \leq 0.5s \\ 1.5 - 0.5 \cdot \cos(2\pi(t - 0.5)) & 0.5s \leq t \leq 1.5s \end{cases} \quad (2)$$

A fluid–solid coupling analysis was performed to evaluate the mechanical effects and deformation of the vascular wall under simulated flow conditions with an inlet pressure of $11208 \cdot f(t)$ Pa and an outlet pressure of $11192 \cdot f(t)$ Pa.

For the vascular sensor based on the triboelectric effect, the tribocharge density (σ_{tribo}) of the PDMS film was set to be $4 \mu\text{C m}^{-2}$. In the initial state, the distance between the two triboelectric layers was 300 μm . The periodic expansion and contraction of the artery alter the air spacer between the triboelectric layers, consequently impacting the potential distribution on the electrodes.

Statistical analysis

Data are reported as the mean \pm SD (standard deviation), with the number of samples (n) indicated. Statistical analysis was performed using Student's t test, and a P value of 0.05 or less is considered statistically significant. Data for box-and-whisker plots were plotted as median with first and third quartiles. Confocal and SEM micrographs were consistent across at least three independently conducted experiments. All the data were analyzed and plotted by ImageJ 1.54 g (National Institutes of Health (NIH), Bethesda, MD, USA), GraphPad Prism v6.01 (GraphPad Software Inc., La Jolla, CA, USA) or Origin (OriginPro 2021C, OriginLab Corporation, USA).

Reporting summary

Further information on research design is available in the Nature Portfolio Reporting Summary linked to this article.

Data availability

All relevant data supporting the key findings of this study are available within the article and its Supplementary Information files. Source data are provided with this paper.

References

- Cannon, B. Biochemistry to behaviour. *Nature* **493**, S2–S3 (2013).
- Hayden, E. C. Cardiovascular disease gets personal. *Nature* **460**, 940–941 (2009).
- Caliskan, E. et al. Saphenous vein grafts in contemporary coronary artery bypass graft surgery. *Nat. Rev. Cardiol.* **17**, 155–169 (2020).
- Seifu, D. G., Purnama, A., Mequanint, K. & Mantovani, D. Small-diameter vascular tissue engineering. *Nat. Rev. Cardiol.* **10**, 410–421 (2013).
- Moore, M. J., Tan, R. P., Yang, N. J., Rnjak-Kovacina, J. & Wise, S. G. Bioengineering artificial blood vessels from natural materials. *Trends Biotechnol.* **40**, 693–707 (2022).
- Niklason, L. E. & Lawson, J. H. Bioengineered human blood vessels. *Science* **370**, 185 (2020).
- Weekes, A. et al. Biofabrication of small diameter tissue-engineered vascular grafts. *Acta Biomater.* **138**, 92–111 (2022).
- McKavanagh, P., Yanagawa, B., Zawadowski, G. & Cheema, A. Management and prevention of saphenous vein graft failure: a review. *Cardiol. Ther.* **6**, 203–223 (2017).
- Zhao, D. X. et al. Routine intraoperative completion angiography after coronary artery bypass grafting and 1-stop hybrid revascularization results from a fully integrated hybrid catheterization laboratory/operating room. *J. Am. Coll. Cardiol.* **53**, 232–241 (2009).
- Thielmann, M. et al. Emergency re-revascularization with percutaneous coronary intervention, reoperation, or conservative treatment in patients with acute perioperative graft failure following coronary artery bypass surgery. *Eur. J. Cardiothorac. Surg.* **30**, 117–125 (2006).
- Michael, S. C. et al. Global vascular guidelines on the management of chronic limb-threatening ischemia. *J. Vasc. Surg.* **70**, 662 (2019).
- Beerkens, F. J. et al. Contemporary coronary artery bypass graft surgery and subsequent percutaneous revascularization. *Nat. Rev. Cardiol.* **19**, 195–208 (2022).
- Kulik, A. et al. Secondary prevention after coronary artery bypass graft surgery: a scientific statement from the American Heart Association. *Circulation* **131**, 927–964 (2015).
- Rodes-Cabau, J. et al. Sealing intermediate nonobstructive coronary saphenous vein graft lesions with drug-eluting stents as a new approach to reducing cardiac events: a randomized controlled trial. *Circ. Cardiovasc. Interv.* **9**, e004336 (2016).
- Escaned, J. Secondary revascularization after CABG surgery. *Nat. Rev. Cardiol.* **9**, 540–549 (2012).
- Tavano, D. et al. Percutaneous coronary intervention in patients with a single remaining vessel. *Am. J. Cardiol.* **99**, 470–471 (2007).
- Rathod, K. S. et al. Prior coronary artery bypass graft surgery and outcome after percutaneous coronary intervention: an observational study from the pan-london percutaneous coronary intervention registry. *J. Am. Heart Assoc.* **9**, e014409 (2020).
- Elbadawi, A. et al. Outcomes of reoperative coronary artery bypass graft surgery in the United States. *J. Am. Heart Assoc.* **9**, e016282 (2020).
- Takagi, H. et al. A meta-analysis of randomized trials for repeat revascularization following off-pump versus on-pump coronary artery bypass grafting. *Interact. Cardiovasc. Thorac. Surg.* **17**, 878–880 (2013).
- L'Heureux, N. et al. Technology Insight: the evolution of tissue-engineered vascular grafts - from research to clinical practice. *Nat. Clin. Pract. Cardiovasc. Med.* **4**, 389–395 (2007).
- Li, J. et al. Multifunctional artificial artery from direct 3D printing with built-in ferroelectricity and tissue-matching modulus for real-time sensing and occlusion monitoring. *Adv. Funct. Mater.* **30**, 2002868 (2020).
- Madhvapathy, S. R. et al. Implantable bioelectronic systems for early detection of kidney transplant rejection. *Science* **381**, 1105–1112 (2023).
- Oresanya, L., Makam, A. N., Belkin, M., Moneta, G. L. & Conte, M. S. Factors associated with primary vein graft occlusion in a multi-center trial with mandated ultrasound surveillance. *J. Vasc. Surg.* **59**, 996–1002 (2014).
- Safar, M. E. Arterial aging–hemodynamic changes and therapeutic options. *Nat. Rev. Cardiol.* **7**, 442–449 (2010).
- Chandrasekhar, A. et al. Tissue perfusion pressure enables continuous hemodynamic evaluation and risk prediction in the intensive care unit. *Nat. Med.* **29**, 1998–2006 (2023).

26. Libanori, A., Chen, G. R., Zhao, X., Zhou, Y. H. & Chen, J. Smart textiles for personalized healthcare. *Nat. Electron.* **5**, 142–156 (2022).
27. Kireev, D. et al. Continuous cuffless monitoring of arterial blood pressure via graphene bioimpedance tattoos. *Nat. Nanotechnol.* **17**, 864–870 (2022).
28. Wang, C. H. et al. Monitoring of the central blood pressure waveform via a conformal ultrasonic device. *Nat. Biomed. Eng.* **2**, 687–695 (2018).
29. Wang, C. H. et al. Continuous monitoring of deep-tissue haemodynamics with stretchable ultrasonic phased arrays. *Nat. Biomed. Eng.* **5**, 749–758 (2021).
30. Fortin, J. et al. A novel art of continuous noninvasive blood pressure measurement. *Nat. Commun.* **12**, 1387 (2021).
31. Franklin, D. et al. Synchronized wearables for the detection of haemodynamic states via electrocardiography and multispectral photoplethysmography. *Nat. Biomed. Eng.* **7**, 1229–1241 (2023).
32. Mathieu, F., Khellaf, A., Thelin, E. P. & Zeiler, F. A. Continuous thermal diffusion-based cerebral blood flow monitoring in adult traumatic brain injury: a scoping systematic review. *J. Neurotrauma* **36**, 1707–1723 (2019).
33. Boutry, C. M. et al. Biodegradable and flexible arterial-pulse sensor for the wireless monitoring of blood flow. *Nat. Biomed. Eng.* **3**, 47–57 (2019).
34. Ouyang, H. et al. A bioresorbable dynamic pressure sensor for cardiovascular postoperative care. *Adv. Mater.* **33**, 2102302 (2021).
35. Shin, J. H. et al. Bioresorbable pressure sensors protected with thermally grown silicon dioxide for the monitoring of chronic diseases and healing processes. *Nat. Biomed. Eng.* **3**, 37–46 (2019).
36. Tang, C. Y. et al. Unconstrained piezoelectric vascular electronics for wireless monitoring of hemodynamics and cardiovascular health. *Small* **20**, 2304752 (2023).
37. Cheng, T., Shao, J. & Wang, Z. L. Triboelectric nanogenerators. *Nat. Rev. Methods Prim.* **3**, 39 (2023).
38. Fleischer, S., Tavakol, D. N. & Vunjak-Novakovic, G. From arteries to capillaries: approaches to engineering human vasculature. *Adv. Funct. Mater.* **30**, 1910811 (2020).
39. Smith, R. J. et al. Endothelialization of arterial vascular grafts by circulating monocytes. *Nat. Commun.* **11**, 1622 (2020).
40. Gupta, P. & Mandal, B. B. Tissue-engineered vascular grafts: emerging trends and technologies. *Adv. Funct. Mater.* **31**, 2100027 (2021).
41. Liu, Z., Wan, X., Wang, Z. L. & Li, L. Electroactive biomaterials and systems for cell fate determination and tissue regeneration: design and applications. *Adv. Mater.* **33**, e2007429 (2021).
42. Damodaran, V. B. & Murthy, N. S. Bio-inspired strategies for designing antifouling biomaterials. *Biomater. Res.* **20**, 18 (2016).
43. Wu, J. J. et al. Adhesive anti-fibrotic interfaces on diverse organs. *Nature* **630**, 360–367 (2024).
44. Feng, L. A., Shi, J., Guo, J. Y. & Wang, S. F. Recent strategies for improving hemocompatibility and endothelialization of cardiovascular devices and inhibition of intimal hyperplasia. *J. Mater. Chem. B* **10**, 3781–3792 (2022).
45. Gupta, P. & Mandal, B. B. Silk biomaterials for vascular tissue engineering applications. *Acta Biomater.* **134**, 79–106 (2021).
46. Gaba, P., Gersh, B. J., Ali, Z. A., Moses, J. W. & Stone, G. W. Complete versus incomplete coronary revascularization: definitions, assessment and outcomes. *Nat. Rev. Cardiol.* **18**, 155–168 (2021).
47. Deng, J., Zhao, C. S., Spatz, J. P. & Wei, Q. Nanopatterned adhesive, stretchable hydrogel to control ligand spacing and regulate cell spreading and migration. *ACS Nano* **11**, 8282–8291 (2017).
48. Yu, L. X. et al. Self-strengthening adhesive force promotes cell mechanotransduction. *Adv. Mater.* **32**, 2006986 (2020).
49. Liu, Z. et al. Cell-traction-triggered on-demand electrical stimulation for neuron-like differentiation. *Adv. Mater.* **33**, e2106317 (2021).
50. Zhi, D. et al. Mechanically reinforced biotubes for arterial replacement and arteriovenous grafting inspired by architectural engineering. *Sci. Adv.* **8**, eabl3888 (2022).
51. Cheng, S. Y. et al. Electronic blood vessel. *Matter* **3**, 1664–1684 (2020).
52. Ren, X. K. et al. Surface modification and endothelialization of biomaterials as potential scaffolds for vascular tissue engineering applications. *Chem. Soc. Rev.* **44**, 5680–5742 (2015).
53. de Vries, M. R., Simons, K. H., Jukema, J. W., Braun, J. & Quax, P. H. Vein graft failure: from pathophysiology to clinical outcomes. *Nat. Rev. Cardiol.* **13**, 451–470 (2016).
54. Akentjew, T. L. et al. Rapid fabrication of reinforced and cell-laden vascular grafts structurally inspired by human coronary arteries. *Nat. Commun.* **10**, 3098 (2019).
55. Wu, W., Allen, R. A. & Wang, Y. Fast-degrading elastomer enables rapid remodeling of a cell-free synthetic graft into a neoartery. *Nat. Med.* **18**, 1148–1153 (2012).

Acknowledgements

This work was supported by the National Nature Science Foundation (Nos. 82202333, Z.L.; 82072065, L.L.; 32171347, D.Z.; 31870969, D.Z.), the Fundamental Research Funds for the Central Universities (E2EG6802X2, L.L.; E2E46801, Z.L.), the China Postdoctoral Science Foundation (Nos. BX2021299, Z.L.; 2021M703166, Z.L.), the Biomaterials and Regenerative Medicine Institute Cooperative Research Project, the Shanghai Jiaotong University School of Medicine (2022LHA04, D.Z.), the Leader of Health Discipline of the Shanghai Health Commission (2022XD038, D.Z.), and the National Youth Talent Support Program (L.L.). The authors thank Prof. Ranran Wang from the Shanghai Institute of Ceramics, Chinese Academy of Sciences and Prof. Chuanglong He from Donghua University for their help in sample fabrication and characterization and Prof. Xinglu Huang from Nankai University for helpful discussion.

Author contributions

Z.L., L.L., D.Z., and Z.L.W. conceived the project. Z.L. and C.T. designed and conducted the experiments. N.H. performed the operation on the cynomolgus monkeys. Z.J. performed the COMSOL simulation. X.L. designed the Bluetooth module. S.W., Q.H., C.X., S.Y., and Z.W. provided supervision and expertise. Z.L. wrote the manuscript. L.L., D.Z., and Z.L.W. revised the manuscript, and all the authors contributed to the discussion and revision of the manuscript.

Competing interests

The authors declare no competing interests.

Additional information

Supplementary information The online version contains supplementary material available at <https://doi.org/10.1038/s41467-025-58056-2>.

Correspondence and requests for materials should be addressed to Zhong Lin Wang, Duohong Zou or Linlin Li.

Peer review information *Nature Communications* thanks the anonymous, reviewers for their contribution to the peer review of this work. A peer review file is available.

Reprints and permissions information is available at <http://www.nature.com/reprints>

Publisher's note Springer Nature remains neutral with regard to jurisdictional claims in published maps and institutional affiliations.

Open Access This article is licensed under a Creative Commons Attribution-NonCommercial-NoDerivatives 4.0 International License, which permits any non-commercial use, sharing, distribution and reproduction in any medium or format, as long as you give appropriate credit to the original author(s) and the source, provide a link to the Creative Commons licence, and indicate if you modified the licensed material. You do not have permission under this licence to share adapted material derived from this article or parts of it. The images or other third party material in this article are included in the article's Creative Commons licence, unless indicated otherwise in a credit line to the material. If material is not included in the article's Creative Commons licence and your intended use is not permitted by statutory regulation or exceeds the permitted use, you will need to obtain permission directly from the copyright holder. To view a copy of this licence, visit <http://creativecommons.org/licenses/by-nc-nd/4.0/>.

© The Author(s) 2025